Purification of MDI Isomers Using Dynamic Falling Film Melt Crystallization: Experiment and Molecular Simulation

Xueying Lian, Peng He,* Liguo Wang, Yan Cao, Kelin Huang, Shuang Xu, Jiaqiang Chen, and Huiquan Li
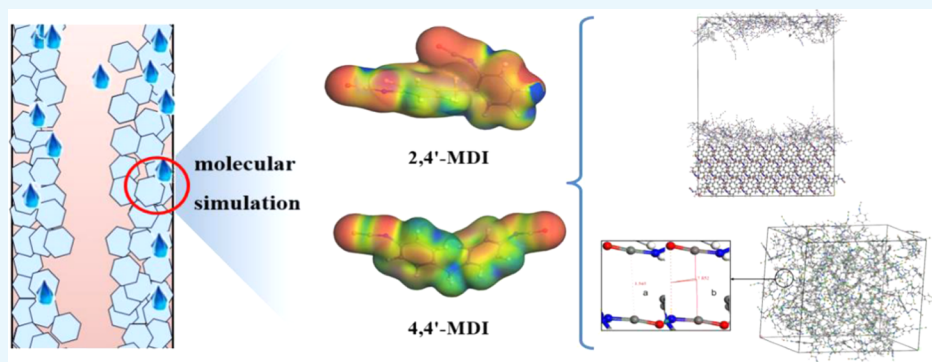
Read Online

ACCESS | Metrics & More | Article Recommendations | Supporting Information

ABSTRACT: In this work, the isomer mixture of 4,4′-diphenylmethane diisocyanate (MDI) and 2,4′-MDI was separated and purified by dynamic falling film melt crystallization, and 99.3% purity and 50.8% yield of 4,4′-MDI could be obtained under optimized conditions. The separation mechanism was simulated by density functional theory (DFT) and molecular dynamics (MD) simulation. Results showed that compared with 2,4′-MDI, 4,4′-MDI molecules could form a more stable and symmetrical crystal structure due to their stronger charge density symmetry and electrostatic potential energy. Furthermore, the separation phenomenon and the formation of the crystal structure were observed according to the radial distribution function (RDF) and orientation correlation function obtained from MD simulation. Finally, the attachment energy (AE) model was used to observe and compare different crystal surfaces; it was proposed that the aggregation of 4,4′-MDI was attributed to the polar attraction between isocyanate groups according to the results of the orientation correlation function. It was also observed that compared with 2,4′-MDI, 4,4′-MDI molecules on the (110) crystal surface were easier to form crystal structures.

1. INTRODUCTION

Diphenylmethane diisocyanate (MDI) with the characteristics of low toxicity, high mechanical strength, and good abrasion resistance is the raw material for polyurethane production,[1] which was widely used in the fields of elastomers, synthetic leather, and polyurethane plastics.[2] However, 2,4′-MDI and 4,4′-MDI isomers were coproduced both in the phosgene and non-phosgene method.[3,4] To obtain pure 4,4′-MDI, namely commercial MDI-100, the separation of 4,4′-MDI from 2,4′-MDI has become a key issue in industrial synthesis of MDI. The molecular structures of 4,4′-MDI and 2,4′-MDI are shown in Figure 1.

Apparently, the separation of 4,4′-MDI and 2,4′-MDI is not easy due to their high similarities in chemical structure, such as boiling point, polarities, and so on. At present, rectification separation is mostly used in industry. Schneider et al. used the distillation separation technology to separate 85.1% 4,4′-MDI from a mixture of 4,4′-MDI, 2,2′-MDI, and 2,4′-MDI. Under the pressure range of 2−50 Mbar and temperature range of 150−250 °C, 4,4′-MDI with a purity of 98.7% was obtained.[5]

Michael et al. also separated 95% 4,4′-MDI from the mixture of 4,4′-MDI, 2,2′-MDI, and 2,4′-MDI using the distillation separation technology under the conditions of 0.1−50 Mbar and 210−225 °C, and results showed that the impurity content in 4,4′-MDI was below 50 ppm.[6] Although rectification separation had achieved industrialization, it has the disadvantages of high energy consumption,[7] high cost, and high requirements in equipment. What is more, 4,4′-MDI and 2,4′-MDI are heat-sensitive materials that self-polymerization occurs easily at high temperature, causing isocyanate loss. Therefore, it is necessary to find a low-temperature, energy-saving, and environmentally friendly method for isocyanate
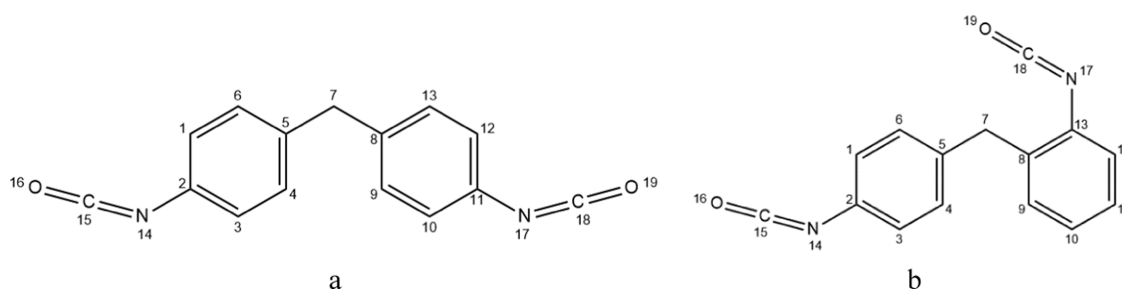
Figure 1. Molecular structures of the isomers. (a) 4,4′-MDI; (b) 2,4′-MDI.

separation to make up for the defects of rectification separation.

Accordingly, the melt crystallization method, which includes static melt crystallization, dynamic falling film melt crystallization, and suspension crystallization, has the advantages of high product purity, energy saving, and low requirements in equipment,[8] was especially suitable for the separation of the heat-sensitive mixtures with similar boiling points.[9−14] In static melt crystallization, because of no mixing device, the melt growth is only caused by natural convection.[15] However, in the process of dynamic falling film crystallization and suspension crystallization, the crystal grows from the well-mixed melt caused by stirring or pumping, leading to high-quality transportation of the crystal surface and the impurities into the melt.[16] Therefore, compared with the static process, the dynamic process has a higher separation efficiency when the crystal growth rate is similar or even faster.[9] Huntsman company used one-time suspension crystallization to increase the purity of 4,4′-MDI from 82 to >99%.[17] The energy consumption is only 30% of the vacuum distillation process. However, the solid and liquid are difficult to be separated in suspension crystallization industrially, and the pipeline will be blocked during the transportation. Comparatively, in dynamic falling film melt crystallization, the above-mentioned problem could be avoided because the crystal grows on the wall of the crystallization tube in the dynamic process, and the liquid flows down to circulate that the solid−liquid separation is not required. In industrial applications, dynamic falling film melt crystallization was used to purify p-xylene from 75 to 99.5%.[18]

On the other hand, the molecular dynamics solid−liquid equilibrium and the crystal surface growth mechanism of the melt crystallization of isocyanate at microscale are still unclear. In recent years, molecular dynamics was used to study the microscopic solid−liquid equilibrium mechanism of solutions. Maeda et al. used the radial distribution function (RDF) to observe the configuration of molecules in the solute crystallization process and used the local composition of the solute (LC) to image the relationship between clusters and nuclei.[19] Li et al. also used the RDF to analyze the solubility of binary systems and pointed out that the intermolecular forces were mainly short-range interactions.[20] Ge et al. used equilibrium and nonequilibrium molecular dynamics methods to simulate the solid−liquid equilibrium phase transition of the single-component Lennard Jones system and successfully obtained the density of the liquid and solid phases separately in the solid−liquid coexistence system.[21] In the above-mentioned examples, the formation of clusters and nuclei during solution crystallization and the density of solid and liquid phases in the solid−liquid coexistence zone were studied by molecular dynamics. However, until now, the study on the molecular dynamics of the solid−liquid phase equilibrium in

melt crystallization has not been reported. The nucleation of 4,4′-MDI and the separation of MDI isomers via the above-mentioned analysis methods will be helpful to clarify the crystal surface growth mechanism in melt crystallization.

Furthermore, the molecular dynamics (MD) method, based on the improved AE model, was also used to predict the crystal morphology of solutes in organic solvents through the calculation of adsorption and crystallization energy.[22,23] Wang et al. used the MD method to predict the concentration in eight pure organic solvents with the crystal morphology of β-HMX (octahydro-1,3,5,7-tetranitro-1,3,5,7-tetrazocine).[24] Lan et al. studied the crystal morphology of hexanitrohexaazaisowurtzitane (HNIW) in vacuum and ethyl acetate using the AE mode.[25] However, in the above-mentioned research, AE model was used to predict the crystal morphology of solutes precipitated in solvents. It is necessary to predict the crystal morphology of 4,4′-MDI by AE model, so as to study the microgrowth mechanism of 4,4′-MDI molecules on the crystal surfaces.

In this paper, dynamic falling film melt crystallization was used to separate 4,4′-MDI and 2,4′-MDI by adopting a dynamic cycle mode. Molecular dynamics simulation was used to explore the mechanism of the melt crystallization of isocyanate. From the perspective of the bond length, bond angle, dihedral angle, and charge density, the differences between the pure 4,4′-MDI, 2,4′-MDI, and their binary mixtures were analyzed. The solid−liquid equilibrium micromechanism of 4,4′-MDI and 2,4′-MDI isomers at different temperatures was studied, and an attempt was made to obtain a microscopic picture of the preferential aggregation of 4,4′-MDI in its isomer mixture. Finally, the growth mechanism of 4,4′-MDI on the crystal surface was explored.

2. EXPERIMENTAL SECTION

2.1. Materials. MDI-100 and MDI-50, industrial grade, were purchased from Wanhua Chemical Group Co., Ltd. Acetone was purchased from Beijing Chemical Works Co., Ltd (purity ≥99.5%, AR). Methanol (purity ≥99.5%, HPLC) and ethanol (purity ≥99.7%, GC) were purchased from Sinophenol Chemical Reagent Co., Ltd.

2.2. Experimental Equipment. The dynamic falling film melt crystallization experiments were carried out in the equipment shown in Figure 2. The dynamic falling film melt crystallizer consists of an overflow groove in the upper part and a double-jacketed tube in the bottom part. The function of the overflow groove is to ensure that the material flows evenly along the inner wall of the crystal tube. The inner diameter of the double-jacketed tube is 20 mm, the outer diameter is 40 mm, and the height is 300 mm. The inner layer of the crystallization tube is used for the crystallization separation of materials, and the outer layer is connected with a thermostatic
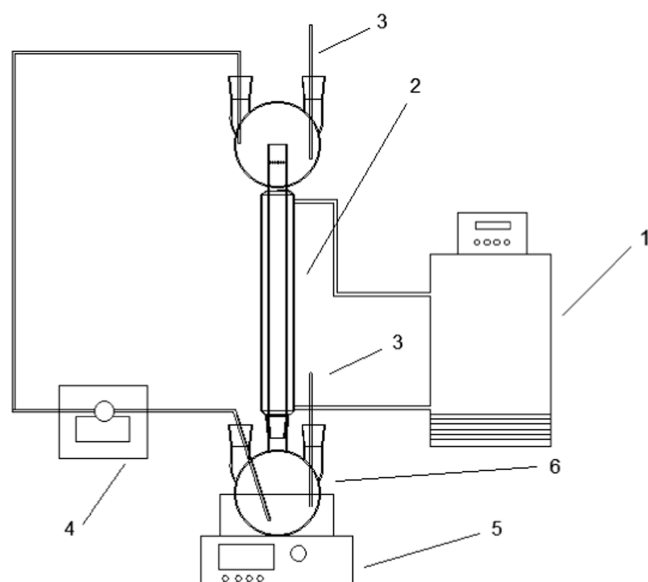
Figure 2. Experimental device. (1) thermostatic water bath; (2) layer melting crystallizer; (3) thermocouple; (4) peristaltic pump; (5) oil bath; and (6) material slots.

water bath (CKDC-3006, Van dillon Technology, Nanjing, China) for temperature control. A peristaltic pump drives the circulation of materials, and an oil bath is used for preheating materials.

2.3. Experimental Procedures. *2.3.1. Binary Phase Diagrams.* The binary phase diagram of binary mixtures with different 4,4′-MDI mass fractions was characterized using a differential scanning calorimeter.[26] The temperature increased from 0 to 50 °C, the heating rate was 5 K/min, and the nitrogen purge was 50 ml/min.

2.3.2. Experiments. The experiment was carried out with a binary mixture of 4,4′-MDI and 2,4′-MDI (233 g), in which 4,4′-MDI accounted for 80% of the mass and the melt recirculation rate was 30 mL/min.

A binary mixture with a high content of 4,4′-MDI was placed in the material tank and reacted using the peristaltic pump. The mixture passed through the pipe to form a crystal film on the inner wall of the crystal tube. The temperature of the thermostatic water bath was controlled at 2−3 °C below the melting point of 4,4′-MDI.

The molten material was poured into the feed tank and conveyed to the top of the crystallization tube through the peristaltic pump and evenly distributed along the inner wall of the crystallization tube. At the same time, the jacketed crystallization tube started linear cooling at a certain rate through the thermostatic water bath. The cooling rate was range from 1−9 °C/h, and the final crystallization temperature was range from 21−27 °C. When the cooling procedure finished, the circulation of the material stopped and the crystallization tube remained at the terminal temperature for 30 min.

Through linear heating at a certain rate, the impurities gradually melted into the material tank, and hence, the crystals on the wall of the crystallization tube were slowly purified. The temperature range was 27−39 °C, and the temperature rate range was 1−6 °C/h.

When the temperature of the thermostatic water bath was increased above the melting point of 4,4′-MDI, the products with high purity on the wall of the crystallization tube were melted and dropped into the material tank. Finally, the samples were weighed, and the purity of 4,4′-MDI was determined by liquid chromatography. The yields were defined as the ratio of the crystal mass to the raw material. It can be calculated by eq 1

$$Y = \frac{m_c}{m_o} \tag{1}$$

where m_c and m_o represents the mass of the crystal layer on the wall surface and feed, respectively.

3. MODEL CONSTRUCTION AND SIMULATION DETAILS

3.1. Force Field. The COMPASS force field[27] was selected to perform the molecular dynamics simulation. The COMPASS force field[27] had proven to be a powerful ab initio force field that can be parameterized based on extensive experimental data and hence can accurately simulate the thermophysical properties and structure of various condensed-phase materials.[28]

3.2. MD Simulation Method. The initial structural file of 4,4′-MDI, used in the calculation of this work, was from reported literature including the lattice parameters $a = 9.974$ (2) Å, $b = 8.331$ (2) Å, $c = 15.199$ (3) Å, $\alpha = 90°$, $\beta = 92.25$ (2)°, $\gamma = 90°$, and the space group C 2/c.[29] The molecular and
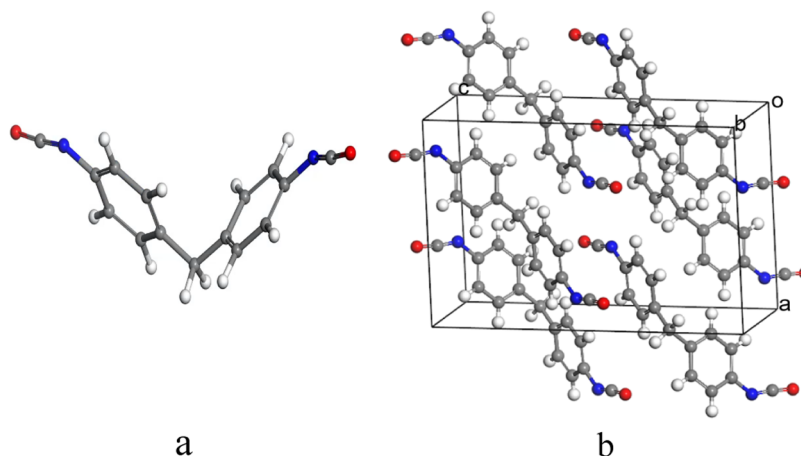

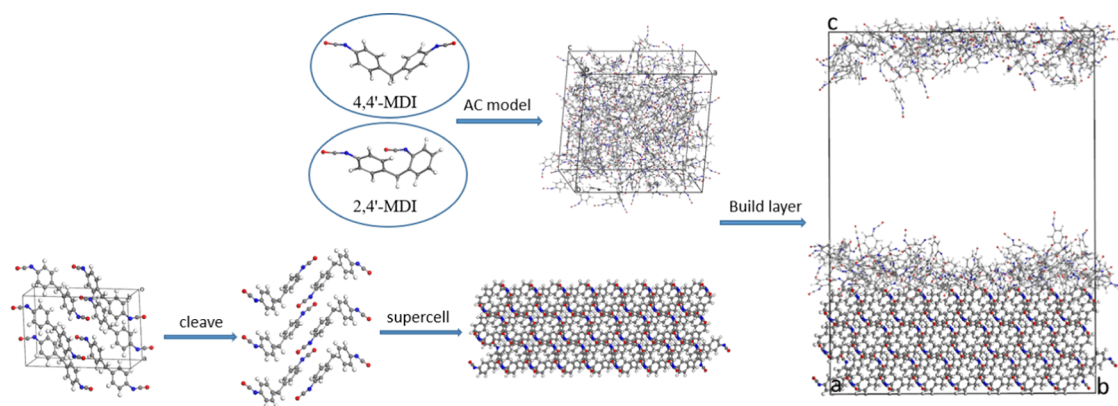**Figure 3.** Molecular structure (a) and unit cell (b) of 4,4′-MDI.

Figure 4. Simple schematic diagram of the entire simulation process.

unit cell structures of 4,4′-MDI are displayed in Figure 3a,b, respectively.

Material Studio[30] software was used to construct 4,4′-MDI and 2,4′-MDI molecules, and the GGA-PW91 basis set[31] was used to optimize the molecules, and then, the electrostatic charges were obtained. The amorphous cells including 4,4′-MDI and 2,4′-MDI molecules were constructed with the amorphous cell module. The COMPASS force field[32] was used to optimize the geometry of the amorphous cell. To make the amorphous cell structure more reasonable, the amorphous molecular model was simulated in an isothermal isobaric ensemble (NPT) using an annealing method in the temperature range from 250 to 500 K.[33] What is more, the MD simulation with a Nose−Hoover thermostat was carried out at the temperature interval of 50 K. To reduce the balancing time, the structure simulated in the previous stage was used as the initial configuration of the MD simulation in the next stage. Two cooling rates including $dT/dt = 1.3 \times 10^{11}$ and 1.4×10^{12} K/s were adopted to study the separation domain.

3.3. Population Analysis Using DFT Methods. All the density functional theory (DFT) calculations were performed using the Dmol3 program available in the Material-studio 2019 package.[34] The generalized gradient approximation (GGA) with the Perdew−Wang 1991 function was used.[35] The following thresholds were used for the geometry optimization: 1×10^{-5} Hartree/Å for the maximum energy change, 2×10^{-3} Hartree/Å for the maximum force, and 5×10^{-3} Hartree/Å for the maximum displacement. The doubled numerical basis set with a set of polarization functions (double numerical plus polarization, DNP) was used, which was comparable to Gaussian 6-31G**.[36]

3.4. Simulation Methods of the Crystal Morphology of MDI. Firstly, the unit cell was constructed according to the XRD data of the 4,4′-MDI crystal in the literature.[29] The morphology of the 4,4′-MDI crystal under vacuum conditions was simulated by AE model[25] in Material Studio software, and the morphologically important surfaces (hkl) were obtained. The crystal surfaces were cleaved, and then, the periodic super structure of each important crystal surface with the length and width of approximately 30 Å was constructed. Secondly, the solvent layers that had 300 randomly distributed solvent molecules at the target density of each solvent were constructed using the amorphous cell module. Accordingly, a simple schematic diagram of the entire simulation process is shown in Figure 4.

3.5. Analytical Methods. *3.5.1. Orientation Correlation Function.* The radial distribution function (RDF) $g(r)$ is a characteristic physical quantity to understand the configuration of solute and solvent molecules. In statistical mechanics, the RDF is a measure of the probability of finding a particle at a distance r away from a given reference particle.[25] $g(r)$ is given in eq 2.[37]

$$g(r) = \frac{1}{4\rho\pi r^2 \xi r} \frac{\sum_{t=1}^{T} \sum_{j=1}^{N} \Delta N(r \to r + \xi r)}{N \times t} \tag{2}$$

where N is the molecule number of the total system; t is the simulation time (ps); r is the difference in the distance; ΔN is number of molecules within the interval of the system; and ρ is density of the molecule system.

3.5.2. Phase Separation Domain. In the process of phase separation, the aggregation of the same particles and the repulsion of different particles will occur in the system, leading to the formation of a phase region with a characteristic phase size gradually. The phase separation takes place, e.g., when a fluid mixture is quenched to the unstable region of its phase diagram. It was recognized that the first r value at which the radial distribution function equals the asymptotic levels, namely equals 1, is found to give the best measure of the average phase size R. Accordingly, the phase separation domain size obtained under different conditions can be used to qualitatively describe the separation effect of melt crystallization under different conditions. As shown in Figure 5, the values in the dotted red line indicate $g(r) = 1$, and the arrow points to the position of $g(r)$, where R is the average phase size.[38−40]

3.5.3. Orientation Correlation Function. As shown in Figure 6, from the unit cell structure of 4,4′-MDI, it was observed that the dihedral angle between two adjacent isocyanate groups of different molecules is 0°, which was considered to be a parallel relationship. The distance of the carbon atoms in the isocyanate groups of the two adjacent molecules is 3.442 Å. If the orientation correlation of isocyanate groups with similar structures in amorphous unit cells was found during the molecular dynamic simulation, it can be considered that the molecules in the amorphous unit cells have formed the crystal structure.

The orientation correlation function $S_t(r)$ is used to describe the correlation degree of two vectors **i** and **j** with distance r. The parallel is 1, and the vertical is −0.5. In isocyanate molecules, vectors **i** and **j** represent isocyanate group vectors in different 4,4′-MDI molecules. The orientation correlation
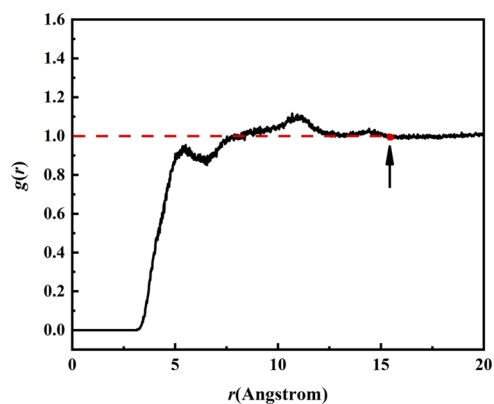
Figure 5. Dimension diagram of the phase separation domain.

Figure 7. Solid−liquid equilibrium data of the 4,4′-MDI and 2,4′-MDI binary mixtures.

function is used to describe the relationship between isocyanate groups in the crystal structure shown in Figure 6. The orientation correlation function $S_t(r)$ is defined as eq 3.

$$S_t(r)=(r) = 0.5(3\langle \cos^2 \theta ij \rangle - 1) \tag{3}$$

where θ_{ij} represents the included angle between two vectors **i** and **j** whose centroids are r apart, which is 0° in parallel and 90° in vertical.

4. RESULTS AND DISCUSSIONS

4.1. Separation of Binary Mixtures of 4,4′-MDI and 2,4′-MDI. The melt crystallization method was mainly composed of crystallization and sweating procedures. It was recognized that the purity of the coarse crystal obtained from crystallization has a great influence on the crystal purity after sweating. Therefore, the operation parameters of cooling rate, final crystallization temperature, sweating rate, and final sweating temperature were investigated in detail.

4.1.1. Analysis of the Binary Phase Diagram. Since pure 2,4′-MDI cannot be obtained in the market, it is impossible to obtain a complete phase diagram of the 2,4′-MDI and 4,4′-MDI isomers. Therefore, only a binary phase diagram with more than 50% 4,4′-MDI could be obtained in Figure 7, and only $W_{4,4'\text{-MDI}}$ (%) is shown in the diagram. It can be seen that with the increase of the 4,4′-MDI content, the freezing point of the mixture gradually increased. Accordingly, the eutectic points are estimated to be below 18 °C, and the mass
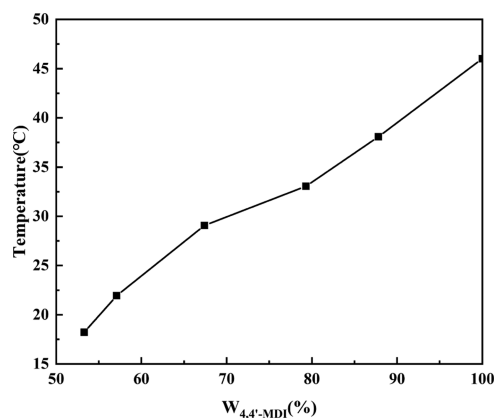
proportion of 4,4′-MDI at the eutectic points should be less than 54%. According to the actual industrial material composition, the simulation liquid of the isomers containing 80% 4,4′-MDI was selected as the initial material for melt crystallization, and the temperature ranged from 25 to 43 °C according to the binary phase diagram.

4.1.2. Effect of Cooling Rate on Coarse Crystal. The effect of different cooling rates on the purity and yield of the coarse crystal was investigated. The results are shown in Figure 8; as can be seen, both of the purities and yields of coarse crystals decreased with the increase in the cooling rate. The driving force of crystallization is the heat and mass transfer, and the transfer rate increases with the cooling rate.[41] Therefore, the increase of the cooling rate led to the rapid growth of crystals. The crystal growth is a typically dendritic growth, the rate of which is too fast that leading to the imperfect crystal growth. Subsequently, the porosity of the crystal layer increased and the pores wrapped with more mother liquor, thus leading to the decrease in crystal purity. However, if the cooling rate increases, the crystallization time is shortened, resulting in a decrease in yield. Considering the yield and purity comprehensively, 1 °C/h was selected as the optimal cooling rate.

4.1.3. Effect of Final Crystallization Temperature on Coarse Crystal. The effect of the final crystallization temperature on the purity and yield of the coarse crystal is
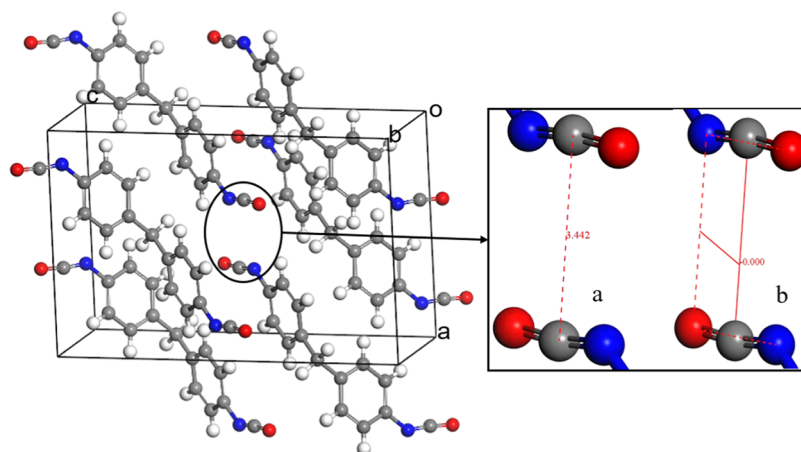

Figure 6. Orientation correlation of adjacent isocyanate groups between different molecules in the 4,4′-MDI crystal structure. (a) Carbon−carbon distance; (b) Dihedral angle.
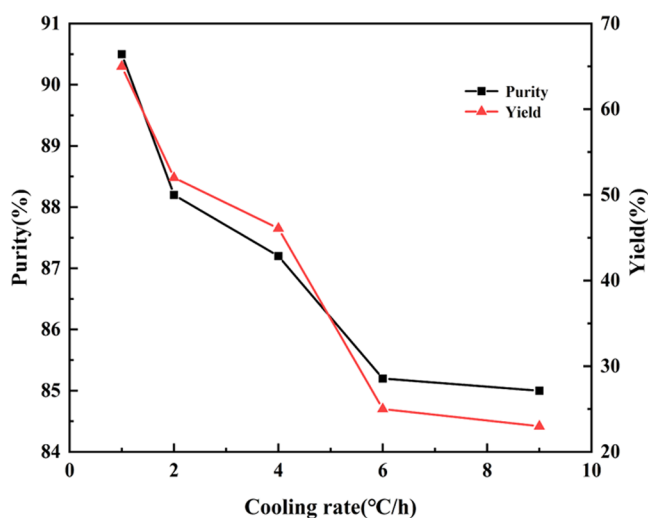
Figure 8. Effect of cooling rate on the purity and yield of the coarse crystal. The initial crystallization temperature is 34 °C; the final crystallization temperature is 25 °C.

shown in Figure 9. As can be seen from Figure 9, with the increase in the final crystallization temperature, the purity of
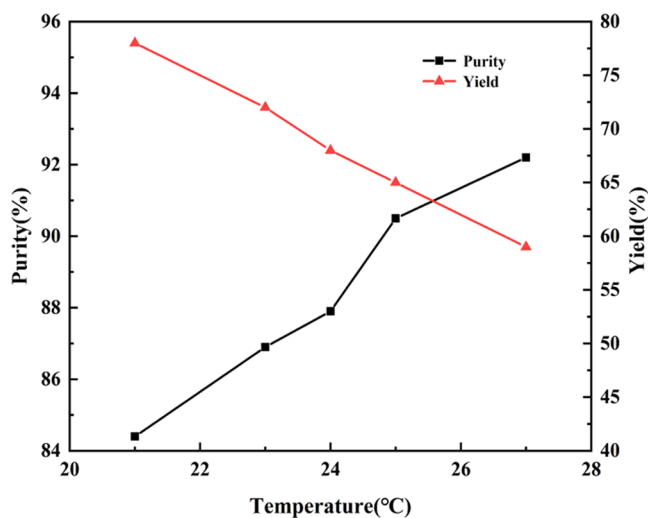

Figure 9. Effect of final crystallization temperature on the purity and yield of the coarse crystal. The initial crystallization temperature is 34 °C; the cooling rate is 1 °C/h.

the coarse crystal increased and the yield decreased. The higher the final crystallization temperature, the smaller the driving force of heat transfer, and thus the slower the crystal growth rate. Hence, the crystal has less inclusions and surface impurities, leading to higher crystal purity. The decrease in the final crystallization temperature would prolong the crystal-lization time and finally lead to the increase of the crystallization rate. Considering both of the purity and yield of 4,4′-MDI, 27 °C was selected as the optimal final crystallization temperature.

4.1.4. Effect of Final Sweating Temperature on the Crystal. Under the aforementioned optimized operating conditions, the influence of the final sweating temperature on the purity and yield of the coarse crystal is shown in Figure 10. As can be seen, the crystal purity is positively correlated with the final temperature of sweating, while the yield is
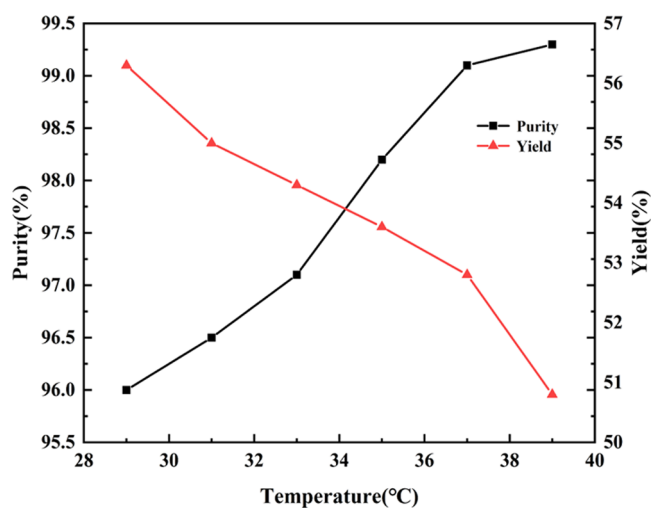

Figure 10. Effect of final sweating temperature on the purity and yield of the crystal. The initial crystallization temperature is 34 °C; the cooling rate is 1 °C/h; and the final crystallization temperature is 27 °C.

negatively correlated. It is deduced that the higher the final sweating temperature, the longer the sweating time, and hence the higher the sweating volume, leading to the increase of the product purity and decrease of the yield. Therefore, on the premise of ensuring a certain yield, the purity of the crystal should be as high as possible, and 39 °C was selected as the optimal final sweating temperature.

4.1.5. Effect of Sweating Rate on the Crystal. The influence of the sweating rate on the purity and yield of the coarse crystal is shown in Figure 11. As can be seen, the purity
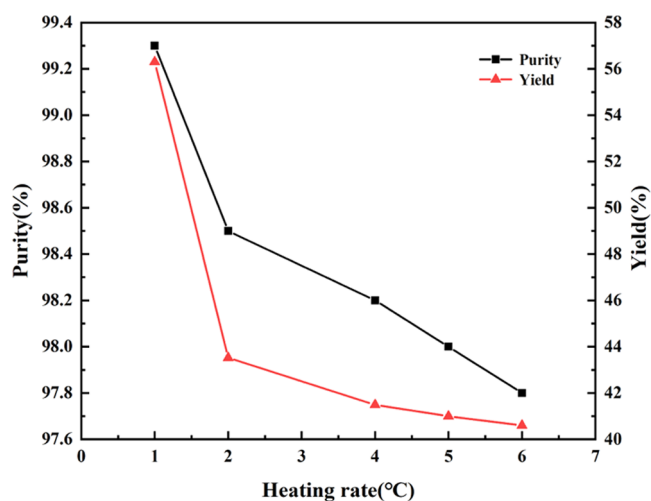

Figure 11. Effect of sweating rate on the purity and yield of the crystal. The initial crystallization temperature is 34 °C; the cooling rate is 1 °C/h; the final crystallization temperature is 27 °C; and the final sweat temperature is 39 °C.

and yield of the crystal were negatively correlated with the sweating rate. The reason is that with the sweating rate accelerated, the stay time of the crystal layer at each temperature would be shorter and the impurities cannot be excluded completely; thus, the crystal purity is reduced. Setting the objective of 4,4′-MDI purity as 99%, 1 °C/h was selected as the optimal sweating rate.

Table 1. Comparison of the Optimized 4,4′-MDI Unit Cell Parameters Based on Different Force Fields

parameter	a (Å)	b (Å)	c (Å)	α (°)	β (°)	γ (°)	total relative error (%)
experiment[29]	9.974(2)	8.331(2)	15.199(3)	90.000	92.250(2)	90.000	
COMPASS	9.581	8.162	16.080	90.000	94.680	90.000	14
UNIVERSAL	10.736	8.263	14.385	90.000	84.432	90.000	22
DREDING	10.911	8.383	14.400	90.000	84.166	90.000	24

To sum up, under the optimized parameters of an initial crystallization temperature of 25 °C, final crystallization temperature of 27 °C, cooling rate of 1 °C/h, final sweating temperature of 39 °C, and sweating rate of 1 °C/h, the purity of the crystal of 4,4′-MDI could reach as high as 99.3% with 50.8% yield.

4.2. Mechanism of Separation of Binary Mixtures of 4,4′-MDI and 2,4′-MDI. According to the experimental results, 4,4′-MDI could be well separated from 2,4′-MDI by the melt crystallization method. However, the solid−liquid equilibrium and crystal growth mechanism were not clear so far. Therefore, in this paper, the population analysis of 4,4′-MDI and 2,4′-MDI molecular structures was carried out by the DFT simulation method to find out the valence bond and electron density distribution differences between the two molecules. Finally, the molecular dynamic simulations of the bulk phase and crystal surface state were carried out in detail, and thus, the solid−liquid equilibrium and crystal growth mechanism were obtained.

First, the comparison of the optimized 4,4′-MDI unit cell parameters based on different force fields with the experimental values[42] is shown in Table 1. As can be seen, the total relative error of lattice parameters between the optimized and experimental values is 14, 22, and 24% for the COMPASS, UNIVERSAL, and DREDING force fields, respectively. It indicated that compared with the UNIVERSAL and DREDING force fields, the COMPASS force field is more suitable for theoretical simulations of the MDI crystal because the optimized lattice parameters of the COMPASS force field are in reasonable agreement with the experimental values.

4.2.1. Population Analysis of the Isomers. The differences in the population analysis between 4,4′-MDI and 2,4′-MDI molecules are shown in Tables S1−S4 in the Supporting Information. Table S1 shows the bond lengths of 4,4′-MDI and 2,4′-MDI molecules calculated by simulation. As can be seen from Table S1, most of the relative differences of bond lengths between 4,4′-MDI and 2,4′-MDI were below 0.4%, whereas the relative differences of C10-C11, C11-C12, C12-C13, and C13-C8 are 0.5, 0.7, 0.6, and 1.1%, respectively, which are relatively larger, indicating that the isocyanate group lengthens the bond length of adjacent C-C on the benzene ring. Table S2 shows the bond angles of 4,4′-MDI and 2,4′-MDI and their relative differences. Most of the relative differences are less than 1%, except C12-C11-N17/C8-C13-N17 and C11-N17-C18/C13-N17-C18, the relative differences of which are 3.4 and 3.5%, respectively. Compared with 2,4′-MDI, 4,4′-MDI has a greater degree of alienation from the right-side isocyanate group than that of the left benzene ring. Thus, there is a spatial repulsion effect between the benzene ring and isocyanate group, which is also proved by the partial dihedral angle calculated by the simulation of 4,4′-MDI and 2,4′-MDI molecules in Table S3. In addition, the isocyanate groups of 2,4′-MDI are more outward than those of 4,4′-MDI, indicating that the interaction force among the 2,4′-MDI molecules is reduced. This might be the reason why the

melting point of 2,4′-MDI (34 °C) is 4−7 °C lower than that of 4,4′-MDI (38−41 °C).

Table S4 shows the partial atomic charge distribution of 4,4′-MDI and 2,4′-MDI molecules, and Figure 12 shows the
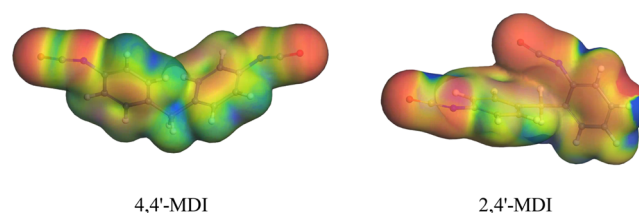
Figure 12. Charge density distribution diagrams of 4,4′-MDI and 2,4′-MDI molecules. Red: Electronegative region. Blue: Electropositive region.

overall charge density distributions of 4,4′-MDI and 2,4′-MDI. It can be seen that the electronegative regions were mainly located in the isocyanate group, while electropositive regions were mainly located in the benzene ring and methylene. From Figure 12, the charge density distribution of 4,4′-MDI was more symmetrical than that of 2,4′-MDI. In addition, it is known that the structure of crystals is symmetric, and it is also reported that the strong symmetry of the molecular structure could promote the transformation of substances to a more orderly crystalline phase.[43] In addition, through the simulation calculation, the absolute value of the electrostatic potential energy of 4,4′-MDI (61.49 kcal·mol⁻¹) is more than two times that of 2,4′-MDI molecules (24.21 kcal·mol⁻¹) at 300 K. Therefore, a higher electrostatic potential energy of 4,4′-MDI could increase the interaction force between molecules and then promote the formation of a symmetrical structure. It means that the structure of the 4,4′-MDI crystal formed is more stable than that of pure 2,4′-MDI and their binary mixed solution. This is the reason why 4,4′-MDI could be separated with high purity through melt crystallization.

4.2.2. Radical Distribution Function. The density variation of the MDI isomer binary mixture between temperatures of 250 and 400 K obtained by the NPT-MD simulation is shown in Figure 13. It can be seen that the density of the mixture had a turning point, which confirmed that crystallization in the solution occurred when the temperature reduced to 300 K.

The RDF is often used to judge the degree of the phase separation in the mixture. If the first arising peak value in the RDF of the mixture is lower than that of the pure component, the phase separation is better.[44] Figure 14 shows the RDF of C7 atoms of 4,4′-MDI and 2,4′-MDI for isothermal simulation from 250 to 400 K. As can be seen, the initial peak positions of the system at different temperatures were between 5.1 and 6.5 Å. At 400 K, the initial peak heights of the pure component and the mixed component of MDI were close to each other, indicating that there is no obvious aggregation behavior occurring between the pure components. From 350 to 325 K, the initial peak of pure components in MDI was higher than that of mixed components, showing that the carbon atoms in
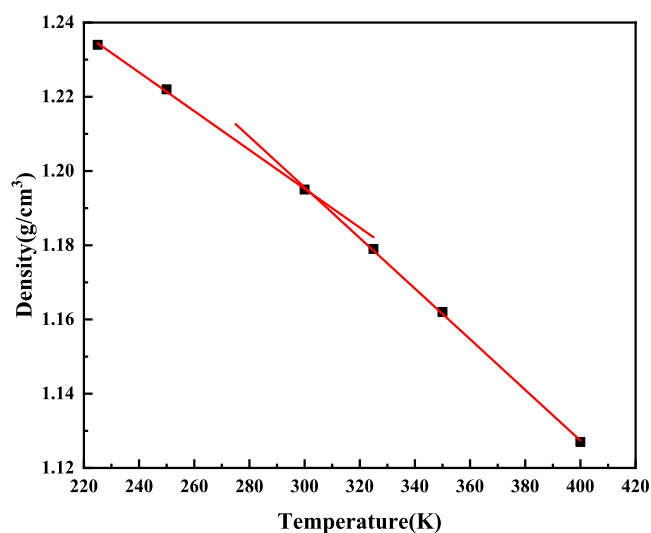
Figure 13. Density variation of the MDI isomer mixture at different temperatures.

the interaction strength between 2,4′-MDI molecules and the surrounding and the limiting effect of 4,4′-MDI molecules. After all, 4,4′-MDI accounts for a large proportion in the number of molecules. As can be seen in Figure 14a, when the temperature is 250 K, the RDF of 4,4′-MDI is relatively smooth, indicating that 4,4′-MDI molecules are more evenly dispersed, and the 2,4′-MDI molecules were limited to a fixed position in the amorphous cells. Furthermore, it can be observed that the initial peak value of the mixture was higher than that of 4,4′-MDI pure components at 250 K. Accordingly, the system is completely crystallized. The aggregation possibility of 2,4′-MDI and 4,4′-MDI molecules is greater than that of single components, and hence, the isomer is difficult to be separated.

To study the effects of the cooling rate on the separation phenomenon in dynamic falling film melt crystallization, the phase separation domain sizes, R of 4,4′-MDI, in the mixture were calculated at different temperatures. According to the solid−liquid equilibrium data in Figure 7, a refrigerating MD simulation was carried out from 320 to 250 K at the cooling rate of 1.3×10^{11} K/s and 1.4×10^{12} K/s, and the results are shown in Figure 15. As can be seen, when the temperature drops from 320 to 300 K, the R value at 1.3×10^{11} K/s cooling rate gradually increases from 9.6 to 16.8 Å, and the R value at 1.4×10^{12} K/s cooling rate gradually increases from 10.1 to 17.3 Å. This is due to the continuous aggregation of 4,4′-MDI molecules.

It is noteworthy that there was a platform in the cooling curve in the temperature range from 320 to 250 K, indicating that if the temperature enters the supercooling range, the change of solid-phase domain size will become slower. It can be also clearly seen that the separation domain sizes in the cooling curves at the rate of 1.3×10^{11} K/s are all larger than those of 1.4×10^{12} K/s, indicating that the separation effect of

different types of molecules tend to avoid intimate interactions with each other on a distance scale of about 5 Å. The carbon atoms instead prefer to interact closely with carbon atoms from the same kind of MDI molecules. In other words, it was indicated that the phase separation occurs between pure components in the binary mixture. It should be noted that the initial peak value of 2,4′-MDI in Figure 14c is 1.2, which is slightly higher than that of 4,4′-MDI. It can be deduced that the degree of aggregation effect between 2,4′-MDI molecules in amorphous cells is stronger. This phenomenon was more obvious in the lower temperature range from 250 to 300 K, in which the mixture is completely solid. It is mainly attributed to
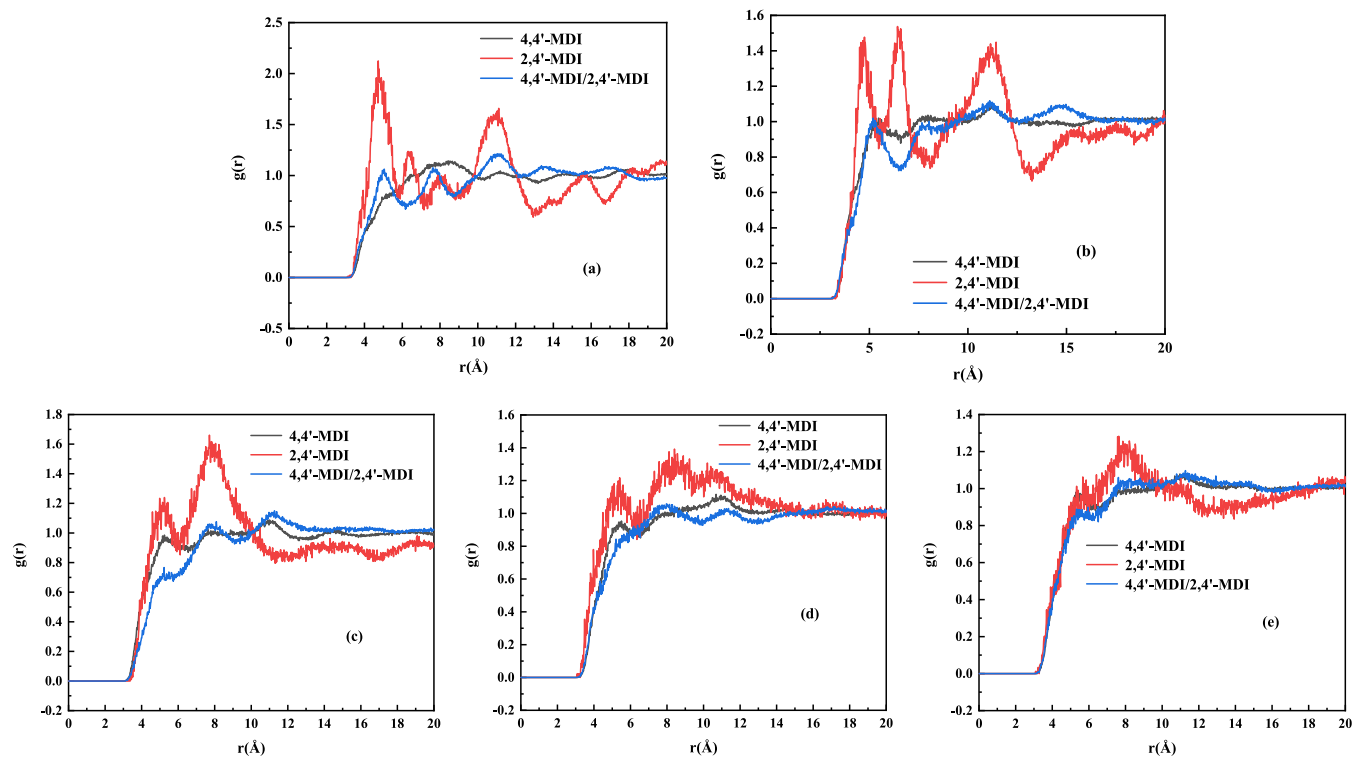

Figure 14. Intermolecular RDF results at 250 K (a), 300 K (b), 325 K (c), 350K (d), and 400 K (e).
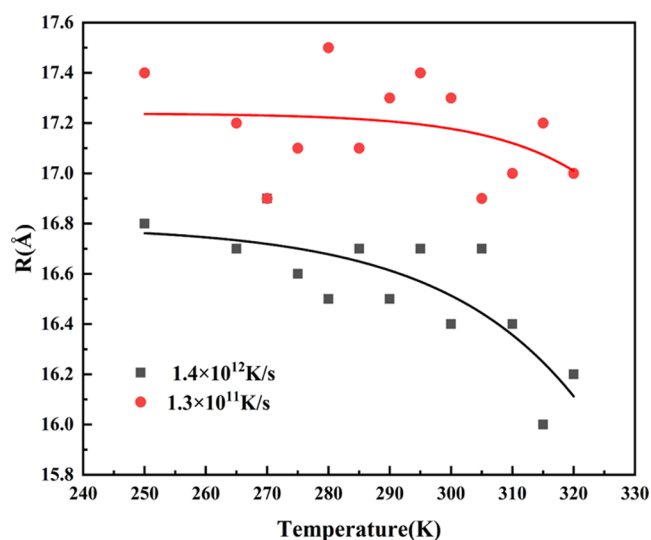
Figure 15. Effect of temperature on the separation domain sizes.

Figure 17. Effect of temperature on the orientation correlation function $S_t(r)$.

4,4′-MDI in the amorphous cell is better at a slower cooling rate. This conclusion was consistent with the results of the melt crystallization experiment qualitatively.

Figure 16 shows the typical molecular configuration image of mixture molecules for the isothermal simulation at 325 K. The localized solute molecules, which are formed below the crystallization temperature of the mixture, are nuclei in the solution. The crystalline structure was formed in the mixture unit cell. The distance between the intermediate C atoms of the adjacent isocyanate groups of two 4,4′-MDI molecules was found to be 3.545 (3) Å, and the dihedral angle was 7.852°. Apparently, this is a significant structural feature of the 4,4′-MDI crystal structure, as shown in Figure 6. Simultaneously, the self-diffusion coefficient of 4,4′-MDI molecules was calculated as 0, which showed the stable crystallization process.

4.2.3. Orientation Correlation Function. The effect of the temperature range from 300 to 450 K on the orientation correlation function is shown in Figure 17. A large value of S_t means a strong correlation in the orientation of the isocyanate groups in MDI molecules at a certain distance. Hence, the probability of forming liquid clusters or crystal nuclei was high in solution. As can be seen, there was a peak near $r = 3.85$ (5) Å, which was consistent with the distance of C atoms of the isocyanate group in the 4,4′-MDI crystal, as shown in Figure 6.
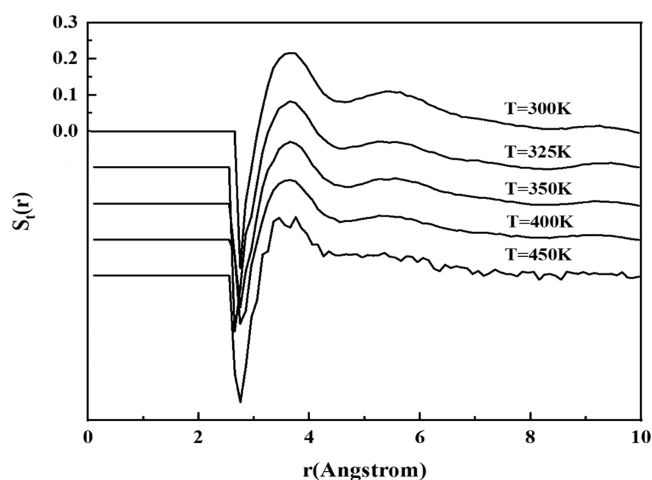
In addition, a marked improvement in the orientation correlation was seen to accompany a decrease in the temperature. This trend is demonstrated more clearly in Figure 18, in which the maximum correlation $S_t(r_{max})$ was
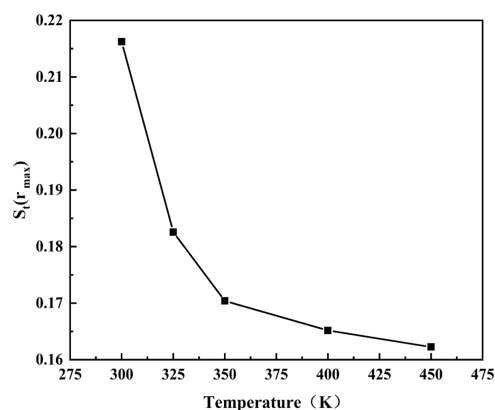

Figure 18. Effect of temperature on the $S_t(r_{max})$ in the intermolecular orientation correlation function.

plotted as a function of the temperature. It can be seen that when the temperature drops from 450 to 325 K, $S_t(r_{max})$ slowly increases from 0.162 to 0.183, and with a continued decrease
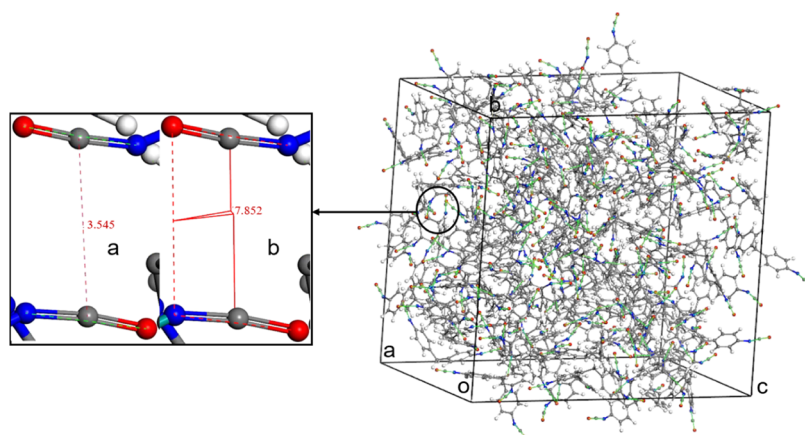

Figure 16. 4,4′-MDI crystal structure in the mixture unit cell at 325 K. (a) Carbon−carbon spacing. (b) Dihedral angle.

in the temperature to 300 K, the $S_t(r_{max})$ increases rapidly to 0.216. This means that with the decrease in temperature, the regularity of the orientation correlation of adjacent isocyanate groups between different molecules is closer to the 4,4′-MDI crystal. Thus, 4,4′-MDI crystals can grow continuously. This also shows that the main interaction force in the 4,4′-MDI crystal structure is among the isocyanate groups of different molecules.

4.2.4. Growth Mechanism of MDI Crystal Surfaces. 4,4′-MDI crystal morphology predicted by AE model and the crystal surface orientations are shown in Figure 19. It can be
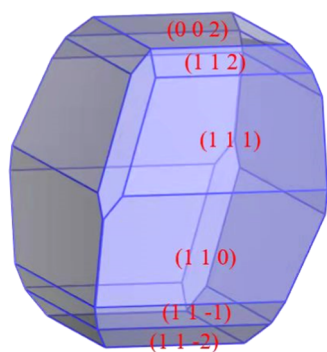

Figure 19. Crystal morphology of 4,4-MDI in vacuum simulated using AE model.

seen that 4,4′-MDI morphology is a monoclinic crystal, and a total of six crystal surfaces of 4,4′-MDI could be oriented, which are (002), (112), (111), (110), (11−1), and (11−2). The attachment energy and area ratio of the six important crystal surfaces of 4,4′-MDI calculated by AE model are listed in Table 2. It can be seen that the area ratios of the most

Table 2. Attachment Energy and Area Ratio of the Six Crystal Surfaces of 4,4′-MDI Calculated by AE Model

surface (hkl)	E_{att} (total)	E_{att} (Vdw)	E_{att} (electrostatic)	area ratio (%)
(110)	−67.355	−60.658	−6.697	32.09
(111)	−64.038	−57.024	−7.014	30.45
(002)	−76.904	−65.799	−11.105	15.42
(11−1)	−83.099	−73.831	−9.268	6.62
(11−2)	−90.455	−82.289	−8.166	6.20
(112)	−73.321	−71.185	−2.136	6.70

important crystal surfaces (110) and (111) are 32.09 and 30.45%, respectively, which are the largest two and consistent with the crystal morphology of 4,4′-MDI in Figure 19. (002) is the third largest surface, which accounts for 15.42%. The area percentage of the (11−1), (11−2), and (112) faces was relatively low at approximately 6.50%.

Also seen from Table 2, the absolute value of attachment energy increased with the decrease in the area ratio of the crystal surface. For example, the area of (110) and (111) is the biggest, whereas their absolute values of attachment energies were the lowest of 67.355 and 64.038 kcal·mol^{-1}, respectively. Also, the area occupied by the crystal surface of (11−2) is the smallest, 6.20%, while the absolute value of attachment energy is the highest of −90.455 kcal·mol^{-1}. This can be interpreted by the growth rate of the crystal surface. The crystal surface with the lowest attachment energy has the greatest influence on the overall morphology of the crystal because it has the

slowest growth rate and is the dominant crystal surface of the crystal.[24]

The molecular arrangements of the crystal surfaces of the MDI crystal are shown in Figure 20. Obviously, the relatively smooth surfaces were (110) and (111), although their isocyanate groups were exposed at different positions and angles on the surface, while the other crystal surfaces were rougher because the isocyanate groups were directly exposed to the surface and almost perpendicular to the surface. According to the rough interface model,[45] the growth rate of the (110) and (111) crystal surfaces is slower than that of other rough crystal surfaces. Therefore, the area occupied by the (110) and (111) crystal surfaces is larger subsequently. This conclusion is consistent with the previous simulation results.

Accordingly, the polarity of the crystal surface can be determined by atoms perpendicular to the crystal surface.[46] From the perspective of crystal surface polarity, the (11−1), (11−2), and (002) crystal surfaces are considered to be strongly polar due to the exposure of the isocyanate group as shown in Figure 20. This can be further proved by the electrostatic part of the adsorption energies as listed in Table 2. The absolute values of electrostatic potential energy of the (11−1), (11−2), and (002) crystal surfaces were 9.268, 8.116, and 11.105 kcal·mol^{-1}, which are relatively larger than those of the other three surfaces. Therefore, it was concluded that the aggregation and growth of 4,4′-MDI molecules on the crystal surface are caused by the attractive force between isocyanate polar groups exposed to the crystal surface.

Furthermore, the orientation correlation function of the C atom between the N atom and O atom in 4,4′-MDI and 2,4′-MDI molecules in the solvent layer at 300 K was observed by selecting the (110) crystal surface. In Figure 6, the distance between the C atom of the isocyanate group in the 4,4′-MDI crystal molecule was about 3.442 Å. Accordingly, the peak value of the orientation correlation function was observed near 3.650 (4) Å. As shown in Figure 21, the $S(r)$ peaks of 4,4′-MDI and 2,4′-MDI were 0.878 and 0.366, respectively. The $S(r)$ peak of 4,4′-MDI (0.878) was significantly 0.512 higher than that of 2,4′-MDI (0.366), indicating that 4,4′-MDI is easier to form a crystal structure on the crystal surface. It is concluded that the nuclei that have a crystalline structure could be distinguished from clusters using the orientation correlation function tools.

5. CONCLUSIONS

In this study, 4,4′-MDI was successfully separated from the mixture of 2,4′-MDI and 4,4′-MDI via dynamic falling film melt crystallization with 99.3% purity and 50.8% yield. The solid−liquid equilibrium and crystal growth mechanisms of 4,4′-MDI and 2,4′-MDI isomers during the melt crystallization were studied via DFT and MD simulation methods. Population analysis results obtained from DFT simulation showed that 4,4′-MDI molecules could form a stable and symmetrical crystal structure due to their stronger charge density symmetry. RDF results showed that 4,4′-MDI pure components could be separated from the isomers at 325 and 350 K. MD simulation of the effect of the cooling rate on the separation of the MDI isomer further proved the conclusions from the experiment. Orientation correlation results showed that compared with 2,4′-MDI, 4,4′-MDI preferentially grows on the crystal surface to form a stable crystal structure. The growth mechanism of the MDI crystal surface simulated via the
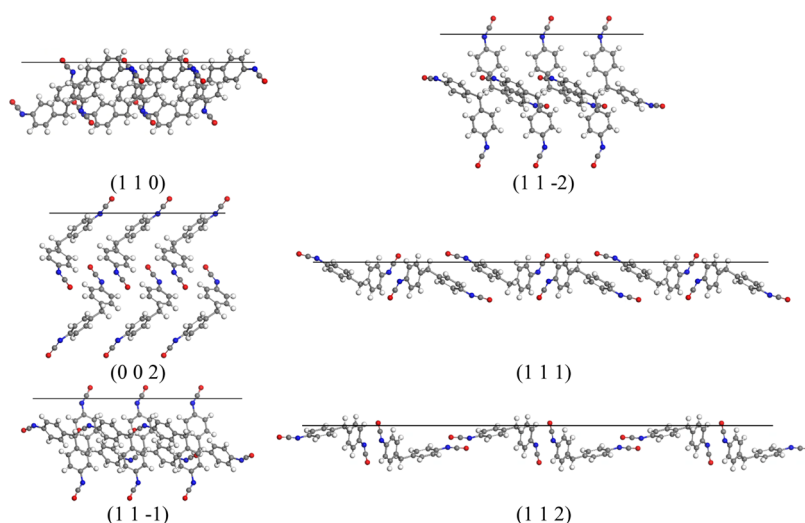
Figure 20. Molecular arrangements of different 4,4′-MDI crystal surfaces.
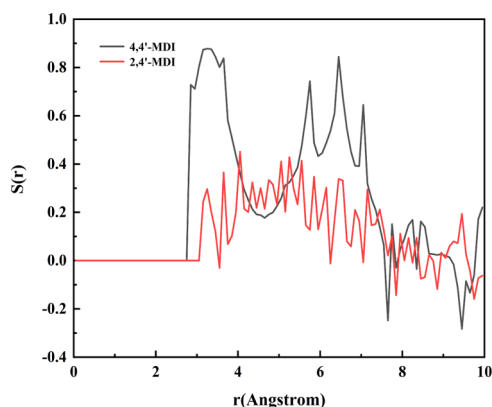

Figure 21. Orientation correlation function of isocyanate groups in 4,4′-MDI and 2,4′-MDI molecules at the crystal surface.

AE model showed that the aggregation of 4,4′-MDI is attributed to the mutual traction between isocyanate polar groups exposed to the crystal surface. In conclusion, falling film melt crystallization is a promising technique to achieve high-efficiency, high-purity separation of the isomers of 4,4′-MDI and 2,4′-MDI, which is suitable for industrialization.

■ ASSOCIATED CONTENT

ⓢ Supporting Information

The Supporting Information is available free of charge at https://pubs.acs.org/doi/10.1021/acsomega.2c01021.

Equilibrium criterion, partial table, and detailed introduction of the population analysis of isomers (PDF)

■ AUTHOR INFORMATION

Corresponding Author

Peng He − *Key Laboratory of Green Process and Engineering, National Engineering Research Center of Green Recycling for Strategic Metal Resources, Institute of Process Engineering, Chinese Academy of Sciences, Beijing 100190, China;* ⓞ orcid.org/0000-0002-1479-8717; Email: phe@ipe.ac.cn

Authors

Xueying Lian − *Guangxi Key Laboratory for Polysaccharide Materials and Modifications, key Laboratory of Chemical and Biological Transformation Process of Guangxi Higher Education Institutes, School of Chemistry and Chemical Engineering of Guangxi Minzu University, Nanning 530006, China; Key Laboratory of Green Process and Engineering, National Engineering Research Center of Green Recycling for Strategic Metal Resources, Institute of Process Engineering, Chinese Academy of Sciences, Beijing 100190, China*

Liguo Wang − *Key Laboratory of Green Process and Engineering, National Engineering Research Center of Green Recycling for Strategic Metal Resources, Institute of Process Engineering, Chinese Academy of Sciences, Beijing 100190, China; Dalian National Laboratory for Clean Energy, Dalian 116023, China*

Yan Cao − *Key Laboratory of Green Process and Engineering, National Engineering Research Center of Green Recycling for Strategic Metal Resources, Institute of Process Engineering, Chinese Academy of Sciences, Beijing 100190, China*

Kelin Huang − *Guangxi Key Laboratory for Polysaccharide Materials and Modifications, key Laboratory of Chemical and Biological Transformation Process of Guangxi Higher Education Institutes, School of Chemistry and Chemical Engineering of Guangxi Minzu University, Nanning 530006, China*

Shuang Xu − *Key Laboratory of Green Process and Engineering, National Engineering Research Center of Green Recycling for Strategic Metal Resources, Institute of Process Engineering, Chinese Academy of Sciences, Beijing 100190, China*

Jiaqiang Chen − *Key Laboratory of Green Process and Engineering, National Engineering Research Center of Green Recycling for Strategic Metal Resources, Institute of Process Engineering, Chinese Academy of Sciences, Beijing 100190, China*

Huiquan Li − *Key Laboratory of Green Process and Engineering, National Engineering Research Center of Green Recycling for Strategic Metal Resources, Institute of Process Engineering, Chinese Academy of Sciences, Beijing 100190, China; School of Chemical Engineering, University of Chinese Academy of Sciences, Beijing 100049, China;* ⓞ orcid.org/0000-0002-3702-3164

Complete contact information is available at:
https://pubs.acs.org/10.1021/acsomega.2c01021

Author Contributions

X.L.: data curation, writing—original draft. P.H.: software, conceptualization, methodology, and validation. L.W.: conceptualization, methodology, and validation. Y.C.: writing—review and editing and supervision. K.H.: writing—review and editing. S.X. and J.C.: experimental design and instruction. H.L.: writing—review and editing.

Notes

The authors declare no competing financial interest.

■ REFERENCES

(1) Li, F.; Wang, Y. J.; Miao, J.; Zhao, X. Q. Progress in Non-Phosgene Synthesis of 4,4′-Diphenylmethane Diisocyanate. *Chem. Ind. Eng.* 2006, 23, 458−462.

(2) Duan, C. W.; You, J.; Liu, B.; Ma, J. L.; Zhou, H. P.; Zhang, H. B.; Zhang, J. Ionic liquids mediated solvothermal synthesis of the 4, 4′-methylenediphenyl diisocyanate (MDI) - an efficient and environment friendly process. *New J. Chem.* 2018, 42, 12243−12255.

(3) Kun-peng, Z. H. Study on the Phosgene Reaction of MDI Industry. *Guangzhou Chem. Ind.* 2010, 38, 63−64.

(4) Gao, J. J.; Zhang, Y.; Li, H. Q. Clean technology for synthesizing diphenylmethane diisocyanate. *Chem. Eng. Process* 2009, 28, 309−315.

(5) Schneider, C.; Zafred, N.; Heussler, A.; Denissen, L.; Koenigsmann, L. Process for preparation and preferably distillative workup of diphenylmethane diisocyanate (MDI). US8703997B22014.

(6) Bock, M.; Thiele, K.; Schelling, H. Process for preparing methylenedi(phenyl isocyanate). US132990392012.

(7) Jia, S.; Gao, Z.; Tian, N.; Li, Z.; Gong, J.; Wang, J.; Rohani, S. Review of melt crystallization in the pharmaceutical field, towards crystal engineering and continuous process development. *Chem. Eng. Res. Des.* 2020, 166, 268−280.

(8) Wu, C.; Cheng, Y.; Wang, L.; Li, X. Solid−liquid equilibrium of dimethyl terephthalate (DMT), dimethyl isophthalate (DMI) and dimethyl phthalate (DMP) in melt crystallization process. *Chin. J. Chem. Eng.* 2017, 25, 1735−1739.

(9) Beierling, T.; Micovic, J.; Lutze, P.; Sadowski, G. Using complex layer melt crystallization models for the optimization of hybrid distillation/melt crystallization processes. *Chem. Eng. Process* 2014, 85, 10−23.

(10) Beierling, T.; Gorny, R.; Sadowski, G. Modeling Growth Rates in Static Layer Melt Crystallization. *Cryst. Growth Des.* 2013, 13, 5229−5240.

(11) Verdoes, D.; Arkenbout, G. J.; Bruinsma, O.; Koutsoukos, P. G.; Ulrich, J. Improved procedures for separating crystals from the melt. *Appl. Therm. Eng.* 1997, 17, 879−888.

(12) Jiang, X.; Hou, B.; He, G.; Wang, J. Falling film melt crystallization (I): Model development, experimental validation of crystal layer growth and impurity distribution process. *Chem. Eng. Sci.* 2012, 84, 120−133.

(13) Berry, D. A.; Ng, K. M. Synthesis of crystallization-distillation hybrid separation processes. *AIChE J.* 1997, 43, 1751−1762.

(14) Ulrich, J.; Bülau, H. C. Melt crystallization. In *Handbook of Industrial Crystallization*, 2002; Vol. 220, pp 161−179.

(15) Le Page Mostefa, M.; Muhr, H.; Biget, A.; Palasari, E.; Fauconet, M. Intensification of falling film melt crystallization process through micro and milli-structured surfaces. *Chem Eng Process* 2015, 90, 16−23.

(16) Jiang, X.; Xiao, W.; He, G. Falling film melt crystallization (III): Model development, separation effect compared to static melt crystallization and process optimization. *Chem. Eng. Sci.* 2014, 117, 198−209.

(17) Koole, J. L.; Zijl, A. D.; Carr, R. H. The method of simultaneously producing different mixtures of diphenyl methane diisocyanate series isomers. CN102171180B, 2014.

(18) Rui, W.; Yanxia, X.; Xingfu, S.; Feike, W.; Jianguo, Y. Separation and Purification of p-Xylene by Falling Film Crystallization. *J. East China Univ. Sci. Techno., Nat. Sci. Ed.* 2019, 45, 528−533.

(19) Maeda, K.; Asakuma, Y.; Fukui, K. Configurations of solute molecules from homogeneous binary solution during crystallization on molecular dynamics simulations. *J. Mol. Liq.* 2005, 122, 43−48.

(20) Li, X.-H.; Ju, X.-H. Molecular Dynamic Simulation of Melting Points of Trans-1,4,5,8-tetranitro-1,4,5,8-tetraazadacalin (TNAD) with Some Propellants. *Chin. J. Chem. Phys.* 2014, 27, 412−418.

(21) Ge, J.; Wu, G.-W.; Todd, B. D.; Sadus, R. J. Equilibrium and nonequilibrium molecular dynamics methods for determining solid−liquid phase coexistence at equilibrium. *J. Chem. Phys.* 2003, 119, 11017−11023.

(22) Lan, G.; Jin, S.; Li, J.; Lu, Z.; Chen, M.; Wu, N.; Chen, S.; Li, L. Molecular dynamics investigation on the morphology of HNIW affected by the growth condition. *J. Energ. Mater.* 2019, 37, 44−56.

(23) Chen, L.; Chen, P.-F.; Li, Z.-Z.; He, Y.-L.; Tao, W.-Q. The study on interface characteristics near the metal wall by a molecular dynamics method. *Comput. Fluids* 2018, 164, 64−72.

(24) Lei, W.; Dong, C.; Hongzhen, L. Crystal Morphology of β-HMX Under Eight Solvents System Using Molecular Dynamics Simulation and Experiment. *Chin. J. Energy Mater.* 2020, 28, 317−329.

(25) Lan, G.; Jin, S.; Li, J.; Lu, Z.; Chen, M.; Wu, N.; Chen, S.; Li, L. Molecular dynamics investigation on the morphology of HNIW affected by the growth condition. *J. Energetic Mater.* 2018, 37, 44−56.

(26) Suping, D.; Xin, H.; Qiuxiang, Y.; Yuyuan, D.; Yunhe, B.; Ting, W.; Hongxun, H. Heat transfer and its effect on growth behaviors of crystal layers during static layer melt crystallization. *Chem. Eng. Sci.* 2020, 233, No. 116390.

(27) Sun, H. COMPASS: An ab initio force-field optimized for condensed-phase applications - Overview with details on alkane and benzene compounds. *J. Phys. Chem. B* 1998, 102, 7338−7364.

(28) Chen, F.; Liu, Y. Y.; Wang, J. L.; Su, N. N.; Li, L. J.; Chen, H. C. Investigation of the Co-Solvent Effect on the Crystal Morphology of β-HMX Using Molecular Dynamics Simulations. *Acta Phys.-Chim. Sin.* 2017, 33, 1140−1148.

(29) Wilson, R. B.; Chen, Y. S.; Paul, I. C.; Curtin, D. Y. Crystal structure and solid-state reactivity of 4,4′-methylenediphenyl isocyanate (MDI). *J. Am. Chem. Soc.* 1983, 105, 1672−1674.

(30) None., Materrials studio. *Chem. Eng. News.* 2000, 78 (23), ibc.

(31) Chen, Y.; Hu, P.; Lee, M.-H.; Wang, H. Au on (1 1 1) and (1 1 0) surfaces of CeO2: A density-functional theory study. *Surf Sci.* 2008, 602, 1736−1741.

(32) Asche, T. S.; Behrens, P.; Schneider, A. M. Validation of the COMPASS force field for complex inorganic−organic hybrid polymers. *J. Solgel Sci. Technol.* 2017, 81, 195−204.

(33) Kim, A. V.; Medvedev, N. N. Melting and homogeneous crystallization of a Lennard-Jones system. *J. Struct. Chem.* 2006, 47, S141−S150.

(34) Chen, Q.; Wang, X.; Yi, P.; Zhang, P.; Zhang, L.; Wu, M.; Pan, B. Key roles of electron cloud density and configuration in the adsorption of sulfonamide antibiotics on carbonaceous materials: Molecular dynamics and quantum chemical investigations. *Appl. Surf. Sci.* 2021, 536, No. 147757.

(35) Spivey, K. Density Functional Theory Studies of Ligand Attachment to Undecagold Clusters. Southern Illinois University: Carbondale, 2007.

(36) Inada, Y.; Orita, H. Efficiency of numerical basis sets for predicting the binding energies of hydrogen bonded complexes: evidence of small basis set superposition error compared to Gaussian basis sets. *J. Comput. Chem.* **2008**, *29*, 225−232.

(37) Su, M.; Zhou, J.; Lu, J.; Chen, W.; Zhang, H. Using Molecular Dynamics and Experiments to Investigate the Morphology and Micro-structure of SBS Modified Asphalt binder. *Mater. Today Commun.* **2021**, *30*, No. 103082.

(38) Velasco, E.; Toxvaerd, S. Computer simulation of phase separation in a two-dimensional binary fluid mixture. *Phys. Rev. Lett.* **1993**, *71*, 388−391.

(39) Wang, H.; Li, X.; Lin, K.; Geng, X. Morphological Simulation of Phase Separation Coupled Oscillation Shear and Varying Temper-ature Fields. *J. Low Temp. Phys.* **2018**, *191*, 153−173.

(40) Singh, A. K.; Chauhan, A.; Puri, S.; Singh, A. Photo-induced bond breaking during phase separation kinetics of block copolymer melts: a dissipative particle dynamics study. *Soft Matter.* **2021**, *17*, 1802−1813.

(41) Jia, S.; Jing, B.; Gao, Z.; Gong, J.; Wang, J.; Rohani, S. Melt crystallization of 2,4-dinitrochlorobenzene: Purification and process parameters evaluation. *Sep. Purif.* **2020**, *259*, No. 118140.

(42) Wilson, R. B.; Chen, Y.-S.; Paul, I. C.; Curtin, D. Y. Crystal structure and solid-state reactivity of 4,4′-methylenediphenyl isocyanate (MDI). *J. Am. Chem. Soc.* **1983**, *105*, 1672−1674.

(43) Ester, D. F.; Williams, V. E. Molecular symmetry effects on the stability of highly ordered smectic phases. *Liq Cryst.* **2018**, *46*, 76−85.

(44) Hashim, N. A.; Mudalip, S. A.; Harun, N.; Man, R. C.; Sulaiman, S. Z.; Arshad, Z.; Shaarani, S. M. Molecular Dynamics Simulation of Mahkota Dewa (Phaleria Macrocarpa) Extract in Subcritical Water Extraction Process. *IOP Conf. Ser.: Mater. Sci. Eng.* **2018**, *358*, No. 012033.

(45) Jackson, K. A. On surface roughness. *Acta Metall.* **1959**, *7*, 747−748.

(46) Chen, G.; Xia, M.; Lei, W.; Wang, F.; Gong, X. A study of the solvent effect on the morphology of RDX crystal by molecular modeling method. *J. Mol. Model.* **2013**, *19*, 5397−5406.